Original Research

Automatic Intra-Subject Registration-Based Segmentation of Abdominal Fat From Water–Fat MRI

Anand A. Joshi, PhD,[1]* Houchun H. Hu, PhD,[1] Richard M. Leahy, PhD,[1] Michael I. Goran, PhD,[2] and Krishna S. Nayak, PhD[1]

Purpose: To develop an automatic registration-based segmentation algorithm for measuring abdominal adipose tissue depot volumes and organ fat fraction content from three-dimensional (3D) water–fat MRI data, and to evaluate its performance against manual segmentation.

Materials and Methods: Data were obtained from 11 subjects at two time points with intermediate repositioning, and from four subjects before and after a meal with repositioning. Imaging was performed on a 3 Tesla MRI, using the IDEAL chemical-shift water–fat pulse sequence. Adipose tissue (subcutaneous—SAT, visceral—VAT) and organs (liver, pancreas) were manually segmented twice for each scan by a single trained observer. Automated segmentations of each subject's second scan were generated using a nonrigid volume registration algorithm for water–fat MRI images that used a b-spline basis for deformation and minimized image dissimilarity after the deformation. Manual and automated segmentations were compared using Dice coefficients and linear regression of SAT and VAT volumes, organ volumes, and hepatic and pancreatic fat fractions (HFF, PFF).

Results: Manual segmentations from the 11 repositioned subjects exhibited strong repeatability and set performance benchmarks. The average Dice coefficients were 0.9747 (SAT), 0.9424 (VAT), 0.9404 (liver), and 0.8205 (pancreas); the linear correlation coefficients were 0.9994 (SAT volume), 0.9974 (VAT volume), 0.9885 (liver volume), 0.9782 (pancreas volume), 0.9996 (HFF), and 0.9660 (PFF). When comparing manual and automated segmentations, the average Dice coefficients were 0.9043 (SAT volume), 0.8235 (VAT), 0.8942 (liver), and 0.7168 (pancreas); the linear correlation coefficients were 0.9493 (SAT volume), 0.9982 (VAT volume), 0.9326 (liver volume), 0.8876 (pancreas volume), 0.9972 (HFF), and 0.8617 (PFF). In the four pre- and post-prandial subjects, the Dice coefficients were 0.9024 (SAT), 0.7781 (VAT), 0.8799 (liver), and 0.5179 (pancreas); the linear correlation coefficients were 0.9523 (liver volume), 0.8760 (pancreas volume), 0.9991 (HFF), and 0.6338 (PFF).

Conclusion: Automated intra-subject registration-based segmentation is potentially suitable for the quantification of abdominal and organ fat and achieves comparable quantitative endpoints with respect to manual segmentation.

Key Words: adipose tissue; fat volume; fat fraction; obesity; registration; segmentation; fat quantification
J. Magn. Reson. Imaging 2013;37:423–430.

THE ACCUMULATION OF abdominal subcutaneous, visceral, and organ (hepatic, pancreatic) fat has adverse effects on health and increases the risks of heart disease, diabetes, metabolic disorders, and certain cancers (1,2). Subcutaneous and visceral adipose tissue (SAT, VAT) volumes and fat content in the liver and pancreas are important quantitative endpoints in obesity research, and MRI has been increasingly used in recent literature to assess and track these endpoints (3–12). Specifically, monitoring changes in these values is critical in longitudinal studies, which require the same subject to be imaged and analyzed repeatedly. Therefore, the ability to rapidly and accurately determine these values at each time point will be beneficial to researchers who are investigating the progression of obesity and assessing the efficacy of intervention in longitudinal studies.

The large size of three-dimensional (3D) abdominal water–fat MRI data, usually on the order of 50–80 contiguous axial slices, a significant image-processing task, one that typically requires manual analysis by a trained evaluator with assistance from commercial software or dedicated programs (13). While prior work has demonstrated the feasibility of semiautomated to near-automated segmentation tools for quantifying the SAT depot in animal and human studies, currently a moderate level of user intervention is still required for the VAT depot and abdominal organs (14–18). These endpoints are particularly challenging as

[1]Ming Hsieh Department of Electrical Engineering, University of Southern California, Los Angeles, California, USA.
[2]Department of Preventive Medicine, University of Southern California, Los Angeles, California, USA.
Contract grant sponsor: NIH; Contract grant number: R21-DK081173; Contract grant number: K25-DK087931.
Drs. Joshi and Hu contributed equally to this work
*Address reprint requests to: A.A.J., Signal and Image Processing Institute, Ming Hsieh Department of Electrical Engineering, University of Southern California, University Park Campus, EEB 426, M/C 2564, Los Angeles, CA 90089-2564. E-mail: ajoshi@sipi.usc.edu
Received June 2, 2010; Accepted August 7, 2012.
DOI 10.1002/jmri.23813
View this article online at wileyonlinelibrary.com.

the depots and organs can vary in shape and size from subject-to-subject. Based on our own experience from over 200 datasets processed at our institution, it takes approximately 1 h of manual segmentation for an experienced evaluator to process and analyze one 3D abdominal MRI dataset. The main limitation of this approach in longitudinal studies is the need to execute such time-intensive workflow for every image set, even for the same subject at two or more time points. An automatic method based on image registration would be attractive and can potentially speed up the segmentation workflow by minimizing the need for manual processing.

Nonrigid image registration has been extensively applied to human brain MRI data (19–22). It has been used to study changes in brain morphology in single subjects over time and across populations by transforming the imaging data to a common coordinate system in which anatomical structures are aligned. Image registration has also been used as the basis for segmentation. The segmentation labels from a reference or baseline dataset can be warped to fit a target dataset, thus efficiently segmenting the target data. In cases where a large training database of labeled scans is available, machine learning approaches such as Bayesian segmentation can be used for determining the labels of subjects automatically (23). Registration-based approaches have been widely used in brain imaging (24–27) and small animal imaging (28,29). Note that a detailed comparison of registration algorithms is presented elsewhere (30).

In this work, a framework is introduced that applies deformable nonlinear registration between 3D abdominal MRI data at two time points. Manual segmentation of the MRI is performed at one time point which serves as a baseline. These baseline manual labels are transferred to the data at a different target time point using automatic registration to generate automatic labels. While several previous reports have presented similar automated registration algorithms, including atlas-based approaches and have reported strong performance metrics for SAT and VAT volumes (31–33), the present work additionally focus on abdominal organs including the liver and the pancreas. We perform manual segmentation of these organs and generate automatic labels for the organs at the images at the target endpoints using the registration-based segmentation. Additionally, we also evaluate the organ-wise accuracy of the automatic labels as well as quantitative fat fraction endpoints. In the next section, we describe our procedure where manually segmented baseline labels from an initial time point are generated and subsequently deformed to achieve automated segmentation of data from the same subject at target time points. The performance of the proposed automated registration-based algorithm is evaluated against manual segmentations performed by a single evaluator.

MATERIALS AND METHODS

MRI Protocol and Data Collection

All data were acquired on a 3 Tesla whole-body human scanner (Signa HDx, 15M4, GE Healthcare, Waukesha, WI), using an investigational research version of the chemical-shift-based water–fat pulse sequence known as IDEAL (Iterative Decomposition with Echo Asymmetry and Least squares estimation) (34). The sequence is based on a 3D spoiled gradient echo with multi-peak spectral modeling of fat and T_2^* correction (35). It was used to minimize T1 weighting, and approximate proton-density contrast (36). All data were acquired with an eight-element torso coil array with the subject lying in the supine position and entering the magnet bore feet first. In all examinations, 60 to 80 axial 5-mm contiguous slices were acquired to provide coverage of the whole abdomen from the top of the liver to at least the L5 vertebrae. The volumetric data were acquired in five to six consecutive breathholds, each lasting 10 to 15 s. In-plane spatial resolution varied from 1.5 to 2.5 mm depending on subject body size with a 160 $\times$ 160 sampling matrix. Other imaging parameters were: flip angle = 5° (to avoid T_1-bias in the fat fraction estimates) (36), bandwidth = $\pm$125 kHz, six echoes, echo train length = 3, echo spacing = 0.8 ms, first-echo = 1 to 1.5 ms, TR = 9 to 11 ms, and two-fold SENSE (37) parallel imaging. Online image reconstruction produced co-registered water-only, fat-only, in-phase, opposed-phase, T_2^* and normalized 0–100% fat fraction image series. All participants provided informed consent and the above protocol was approved by the local ethics and review board. Two separate sets of MRI experiments were performed:

Dual Time Point Data (REPOS)

In 11 subjects, the 3D IDEAL protocol was implemented twice with intermediate repositioning. Between the scans, both the subject and torso coil array were completely removed from the scanner. The goal of this repositioning (REPOS) was to mimic data collection at two longitudinal time points but with no change in abdominal and organ fat quantities.

Pre- and Postprandial Data (MEAL)

In four additional subjects, the MRI protocol was implemented twice with intermediate repositioning and consumption of a meal. The first scan was performed in the morning, after overnight (>8 h) fasting. The second scan was performed approximately 1 h postprandial. The meal consisted of a sandwich and yogurt, although it was not standardized. The goal of this exercise was to determine the impact of stomach and abdominal distention on the proposed automatic registration-based segmentation algorithm. As in the REPOS exercise, we did not anticipate any absolute change in abdominal and organ fat quantities due to meal intake.

Manual Segmentation

A single evaluator performed manual segmentation of all datasets using a commercial image analysis software package (Magog, Quebec, Canada) to obtain the following quantitative endpoints: volumes of SAT, VAT, liver, and pancreas, as well as hepatic (HFF) and

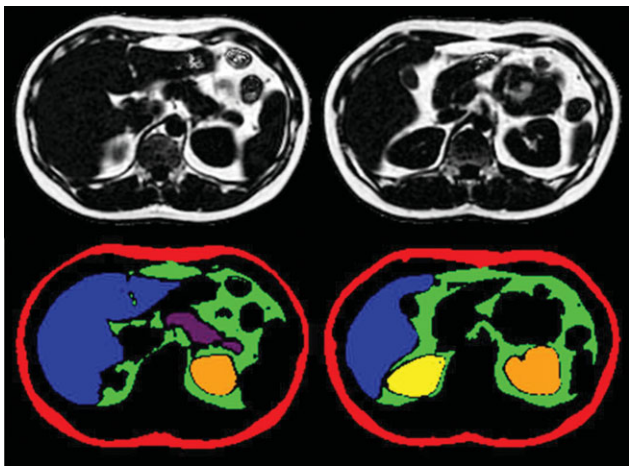

Figure 1. Two representative axial slices: gray-scale fat fraction (top) and corresponding manually segmented labels (bottom) are shown. Fat fraction is displayed on a scale from 0% (black) to 100% (white). Segmentation labels are: red, SAT; green, VAT; blue, liver; purple, pancreas. The kidneys are also shown for illustration (yellow/orange). [Color figure can be viewed in the online issue, which is available at wileyonlinelibrary.com.]

pancreatic (PFF) fat fraction measures. The tool is widely used by investigators in body composition and obesity research (13). For the REPOS data, a total of 22 3D datasets were acquired and analyzed (11 subjects, 2 time points each). The evaluator performed two independent series of segmentations on these 22 datasets to generate intra-operator repeatability metrics. Thus, a total of 44 segmentations were produced from REPOS data. During the independent repeat analysis, the operator did not refer to the previous segmentation results. Furthermore, the order in which the datasets were segmented was randomized and analysis was performed on different days. The average time needed to segment each 3D dataset was approximately one hour. This repeat analysis was used to establish performance benchmarks. For the MEAL data, the operator performed two segmentations per subject, one for the image series acquired in the fasting state, and one for the image series acquired after meal consumption. For all image segmentations, SAT, VAT, liver, pancreas, and additionally the kidneys (for reference) were manually labeled. Figure 1 illustrates representative examples from one of the datasets used in this study. Orthogonal views are shown in Figure 1a. Figure 1b shows two axial slices, along with corresponding manually segmented labels generated using software.

Intensity Correction

Two forms of undesirable signal intensity variations are introduced during the MRI data acquisition process. The first is caused by the imperfect RF excitation, which produces signal-intensity variations along the superior/inferior direction, corresponding to the slab excitation profile of the time-bandwidth limited RF pulses used in each 3D breathhold volume. We retroactively corrected for this signal variation in the data by normalizing to a signal profile measured in a homogeneous gel phantom obtained using the same protocol.

The second form of intensity variation is due to receiver coil sensitivities from the eight-element torso array. We retroactively corrected for this variation by estimating a bias map from the proton density weighted in-phase image series (38). After excluding background air for each slice, voxels with signal intensities in the top 50 percentile were set as the anchor points for a 2D b-spline fit (38,39). The reciprocal of the resultant slice-by-slice fitted b-spline bias maps was applied separately to the water and fat image series to yield signal-intensity corrected data for further registration.

Volume Registration-Based Segmentation

Registration of the intensity-corrected datasets is subsequently performed for each of the 22 REPOS volumes (11 pairs) and the 8 MEAL volumes (4 pairs). A rigid registration was first applied to correct for bulk rotations and translations. A nonrigid registration was then performed using b-splines based on previously described methods (39–41).

Water and fat images were selected for registration in the present work. Alternatively, normalized fat fraction images, which do not suffer from RF transmit and receive signal inhomogeneities, could have also been chosen. We initially used fat fraction images but found areas with low signal (background, air, gas) to be problematic and difficult to mask. We achieved better performance using intensity-corrected fat and water images. Let us denote the fat volumes of the subject by $F_B(x,y,z)$ and $F_T(x,y,z)$, for time point 1 (baseline) and time point 2 (target) respectively. Similarly, let us denote the two water volumes by $W_B(x,y,z)$ and $W_T(x,y,z)$. Furthermore, let the transformation $T(x,y,z)$ represent a deformation map that links any point in the baseline volume to its corresponding point in the target volume. The 3D deformation field $T(x,y,z)$ is represented using a cubic b-spline basis with uniformly spaced knots.

The smoothness of the deformation is measured by a generalization of the elastic energy in 3D given by $C_{smooth}(T) = \iiint [\nabla^2 + \gamma\nabla(\nabla\cdot)]T(x,y,z)dxdydz$ (41). This expression simplifies due to b-spline basis and has a closed form which is a function of spline control vertex coefficients (35,36). The coefficient $\gamma = 0.2$ was used for the results presented here.

The following cost function was used to measure dissimilarity in the matched images:

$$C_{rms}(F_B, F_T, W_B, W_T, T) = \iiint \|F_T(x,y,z) - F_B(T(x,y,z))\|^2 dxdydz + \iiint \|W_T(x,y,z) - W_B(T(x,y,z))\|^2 dxdydz.$$

In this cost function, equal weight was assigned to errors in the fit of water and fat images. The

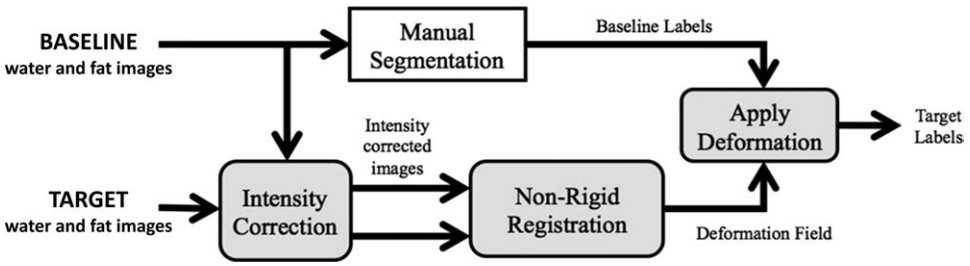

Figure 2. Flow chart of the automated registration-based segmentation approach. Baseline and target datasets each consist of perfectly registered 3D volumes representing fat and water signals. Both datasets undergo intensity correction, including bias-field correction and slab profile correction, before nonrigid registration. The output of registration is a deformation field, which is then applied to the manual segmented labels from the baseline dataset. The end result is a deformation field (one-to-one mapping) between baseline and target datasets, and a set of automatically generated labels for the target dataset.

dissimilarity measure was combined with the smoothness regularizer to form the total cost function $C_{rms}(F_B, F_T, W_B, W_T, T) = C_{smooth}(T)$. This function was minimized using the L-BFGS optimization scheme described in (42). L-BFGS is the low memory version of the Broyden-Fletcher-Goldfarb-Shanno (BFGS) quasi-Newton method that has been shown to perform well for image registration (42).

Figure 2 shows a flowchart summarizing our volume registration-based segmentation algorithm. The intensity-corrected baseline and target datasets are inputs. The output is the deformation field T(x,y,z) that defines the point-by-point correspondence between the baseline and target volumes. This deformation field is subsequently applied to the baseline segmentation labels to generate automatic labels for the target volume. As described in more detail in the following section, automatic labels are then compared and evaluated for quantitative fat accuracy against manually segmented labels of the target volume.

Evaluation

The Dice coefficient (DC) metric (43) was used to assess the degree of overlap and similarity between segmentation labels or sets. They range from 0 to 1, where 0 indicates that there is no overlap and 1 signifies perfect overlap between the two sets. The coefficients were computed for manual segmentation versus registration-based automatic segmentation in both REPOS and MEAL cohorts. Additionally, benchmark DCs were computed for the repeatability analysis in the REPOS data.

SAT, VAT, liver, and pancreas volumes were easily computed for each manual and automated label set by summing the total number of corresponding voxels and multiplying by the voxel resolution. HFF and PFF were estimated by segmenting the organs manually on the IP, OP, water, and fat series first, and transferring the labels to the corresponding fat fraction image to obtain distribution values. For the automatically registered labels, the labels were reloaded and overlaid atop the fat fraction images to obtain the distribution values. Linear regression was used to evaluate the level of agreement between each of the estimated volume and fat fraction quantities. Pearson correlation coefficients were computed for all comparisons.

RESULTS

Table 1 contains demographic information for the all of the REPOS and MEAL subjects. Figure 3 contains representative axial slices from one MEAL dataset and illustrates the significant expansion of the stomach and displacement of surrounding organs and adipose tissues due to food intake. Figure 4 illustrates the effectiveness of the 2D slice intensity correction scheme. Figure 4a and 4b shows water and fat images before and after intensity correction, respectively. Figure 4c contains histograms of fat signal for SAT and VAT depot before and after correction. The histograms for other organs were similar. There was approximately three-fold reduction in the coefficients of variations (standard deviation / mean) for fat and water images after the correction. The intensity correction and registration-based segmentation algorithm was implemented in Matlab and took approximately 15 min of computation time per dataset on a computer with Intel Core 2 2.8 GHz processor, memory.

Figure 5 illustrates a representative result from the registration-based automated segmentation. Axial and sagittal views from one REPOS subject are shown. In Figure 5a, manually segmented color labels from the baseline volume are overlaid atop the target dataset. As expected, before registration, there is a significant mismatch between the labels and the underlying grayscale data, as evidenced in the SAT depot (red), VAT depot (green), and liver (blue). Figure 5b shows the deformation field generated by the registration algorithm displayed by warping a regular grid. Figure 5c highlights the deformed baseline labels. Note that

Table 1
Subject Demographics and Anthropometric Measures of Study Cohort

	Age (yr)	Weight (kg)	Height (cm)	BMI
REPOS (n=11)	39.5	76.16	166.2	27.3
Mean (SD)	(11.0)	(17.0)	(13.1)	(3.7)
MEAL (n=4)	32.5	75.6	172.8	24.9
Mean (SD)	(1.7)	(14.3)	(10.8)	(2.0)

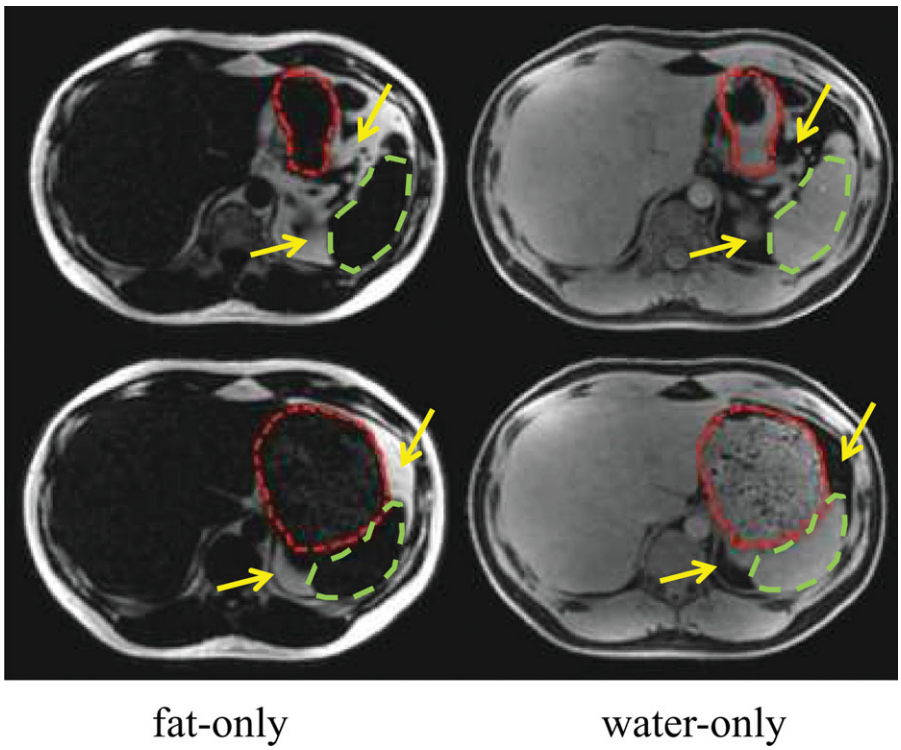

Figure 3. Co-registered axial fat and water images from one volunteer (top) pre-prandial and (bottom) post-prandial. After a meal, the stomach (red dotted) is distended and displaces the spleen (green) and a substantial amount (see arrows). [Color figure can be viewed in the online issue, which is available at wileyonlinelibrary.com.]

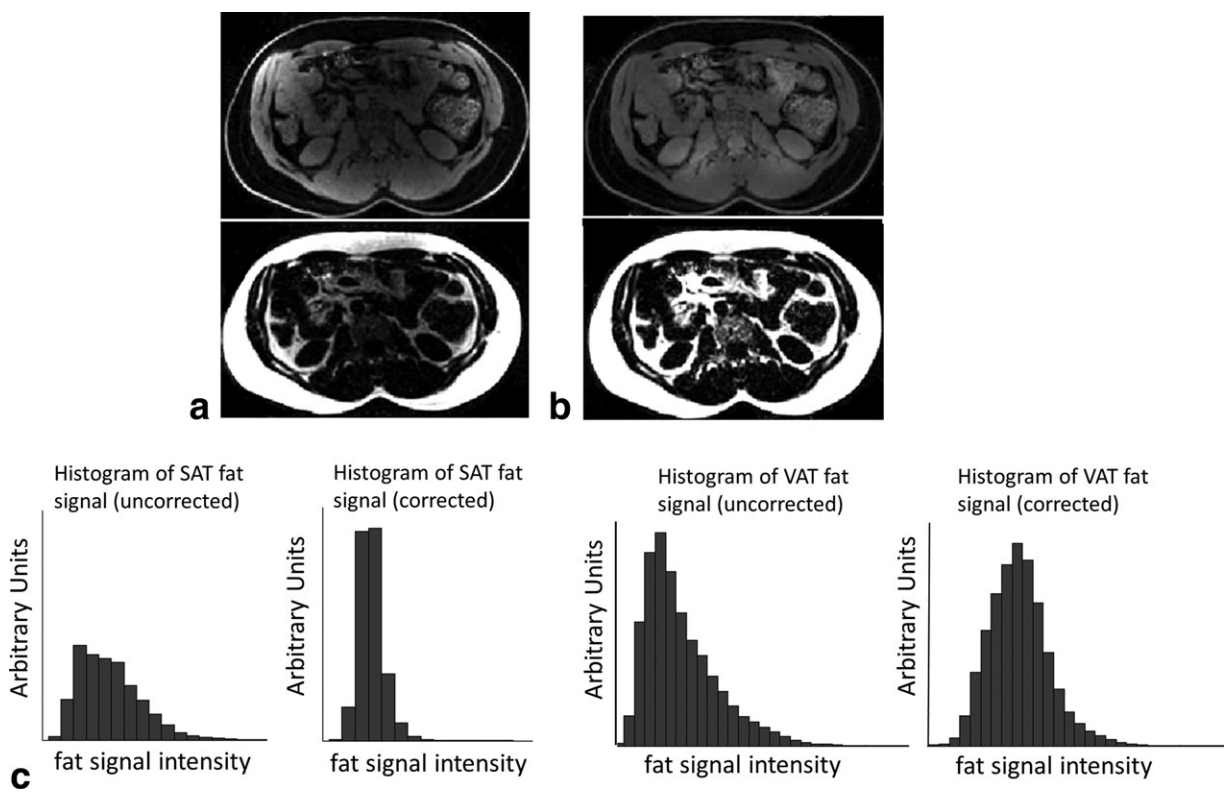

Figure 4. Axial slice water and fat images before (**a**) and after (**b**) bias field correction. **c**: Histograms of fat signal for SAT and VAT before and after bias field correction.

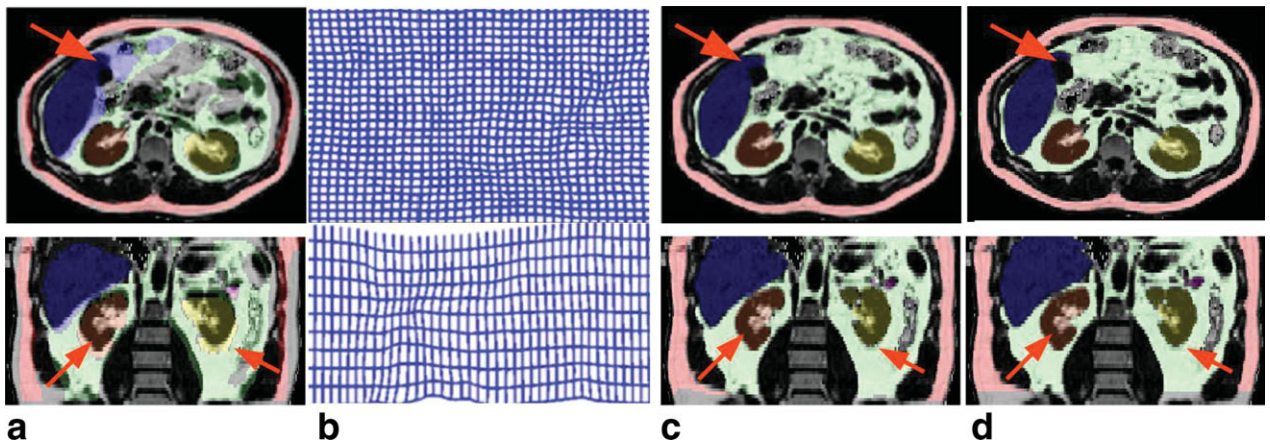

Figure 5. Representative results from one volunteer. All underlying gray scale images are from the "target" time point. **a**: Overlay of baseline labels shows large-scale mismatches in the SAT, VAT, and multiple organs (arrows). **b**: Computed deformation field that maps equivalent positions in the baseline and target volumes (to be applied to baseline labels). **c,d**: Overlay of warped baseline labels, showing accurate segmentation of the abdominal adipose tissue depots and organs (c) in comparison to manual segmentation of the target dataset (d). Segmentation labels: Red, SAT; Green, VAT; Blue, Liver. Labels for kidneys also shown highlight the effectiveness.

nearly all of the mismatches have been resolved. For comparison, Figure 5d contains manually segmented labels from the target volume.

Table 2 summarizes the distribution of DCs for the REPOS and MEAL cohorts. Values are reported for a comparison between repeat manual segmentations by a single operator (e.g., benchmark), and between manual and automated segmentations. For the REPOS cohort, intra-operator performance demonstrated a very high level of agreement for SAT, VAT, and the liver, but not the pancreas. A good level of agreement was achieved between manual and automated segmentations for SAT and the liver. The corresponding DCs were within 10% of the performance benchmarks set by the intra-operator exercise. In the MEAL cohort, the performance of automated segmentation was comparable to that of the REPOS cohort.

Table 3 reports individual average tissue volumes for SAT, VAT, liver, and pancreas, as well as average HFF and PFF values. The average absolute difference between manual and automatic measurements of HFF and PFF were 0.4674 and 2.76, respectively. Table 4 reports the Pearson linear correlation coefficients for the six quantitative fat endpoints (SAT volume, VAT volume, liver volume, pancreas volume, HFF, and PFF) from the REPOS and MEAL cohorts. A high level of performance was detected for both the manual and the automatic method. The MEAL cohort was more challenging in terms of registration because of the significant expansion of stomach and shifting of surrounding organs. The performance of the automatic method was good showing robustness of the method, except for in the pancreas.

DISCUSSION

This study suggests the feasibility of using automated image registration methods for the segmentation of adipose tissue depots and organs from 3D abdominal fat–water MRI. This type of approach is immediately applicable to longitudinal studies in which a baseline time point can be analyzed fully using manual techniques and labels propagated to future time points for tracking of relevant fat distribution measures. The performance of the automated segmentation process was only slightly worse than the repeatability of manual segmentation, for the SAT depot, the VAT depot, and the liver.

The performance of automated segmentation was significantly worse in the pancreas than in the other regions of interest. This is likely due to the fact that the pancreas is small in volume and is surrounded by visceral fat. Consequently, small inaccuracies in its labeling could lead to erroneous inclusion of fat voxels

Table 2
Average Dice Coefficient and Standard Deviations (in Parentheses) Between Segmentation Labels for Subcutaneous Adipose Tissue (SAT), Visceral Adipose Tissue (VAT), Hepatic Fat Fraction (HFF), and Pancreatic Fat Fraction (PFF)*

		SAT	VAT	HFF	PFF
REPOS (n=11)	Manual vs. manual	0.9747 (0.0146)	0.9424 (0.0348)	0.9407 (0.0111)	0.8205 (0.1112)
	Manual vs. automated	0.9043 (0.0622)	0.8235 (0.0943)	0.8942 (0.0453)	0.7168 (0.1338)
MEAL (n=4)	Manual vs. automated	0.9024 (0.0235)	0.7781 (0.066)	0.8799 (0.0333)	0.5179 (0.2300)

*For the REPOS cohort, intra-operator performance metrics are reported for each data set at each of the two time points were independently analyzed twice. These values serve as reference benchmarks. For both REPOS and MEAL cohorts, the performance of the automated algorithm is shown.

Table 3
Measured Adipose Tissue Volumes, Organ Volumes, and Organ Fat Fractions Average and Standard Deviation (in Parenthesis) for the REPOS and MEAL Cohorts

		SAT volume (ml)	VAT volume (ml)	Liver volume (ml)	Pancreas volume (ml)	Hepatic fat frac (%)	Pancreas fat frac (%)
REPOS (n=11)	Manual	3836.20 (1335.86)	2371.59 (1385.34)	1483.05 (343.87)	39.38 (12.80)	7.54 (5.21)	5.16 (2.72)
	Automatic	3748.66 (1443.98)	2364.94 (1387.41)	1425.51 (349.67)	40.37 (14.40)	7.95 (5.18)	5.03 (4.63)
MEAL (n=4)	Manual	3670.87 (1573.83)	1555.95 (756.52)	1106.68 (247.74)	33.39 (15.25)	5.43 (2.79)	5.10 (2.60)
	Automatic	3554.29 (1360.15)	1497.99 (760.84)	1100.06 (294.14)	39.51 (17.93)	5.83 (2.90)	5.24 (4.84)

and overestimation of the organ's fat fraction. This makes its delineation even by manual segmentation challenging and such difficulties were evident in the results from the manual evaluator (Table 2). Additional work is needed for more accurate manual and automated segmentation of the pancreas. It is worth noting that, while it takes an experienced operator approximately 45 to 60 min to manually segment the full dataset, and a majority of time is spent on the large adipose tissue depots and the liver. If segmentation of small organs such as the pancreas remains a problem, one may consider using automated segmentation for the large fat depots and liver, as that has been demonstrated to be reliable, and rely on manual segmentation for the pancreas. We note that in addition to the segmentation time required for manually delineating the organ boundaries, the manual rater needs to be trained for this purpose, especially if accurate organ segmentation is required. Additionally, inter-rater error is introduced when scans are segmented by multiple manual raters. Notwithstanding the various tradeoffs in automated and manual approaches, investigators can decide to use an appropriate approach based on performance benchmarks presented in this study. The present study demonstrates feasibility of the proposed automated method. Logically, the next step in experiments is to test the proposed automated method in a real longitudinal study, while maintaining the use of manual segmentation (as ground truth) to assess tradeoffs in accuracy and time.

Dice coefficients were used as a metric to quantify the amount of overlap between the warped baseline and manually generated target labels. Dice coefficients have been used often for evaluating the accuracy of registration methods because they provide a quantitative measure of registration accuracy, ranging from 0 to 1, corresponding to no overlap and complete overlap, respectively. They are also easy to compute. However, any overlap measure, including the Dice coefficient, can be particularly sensitive to misregistration of thin structures, which possibly accounts for the fact that our results were worse for smaller organ ROIs. This is because for such structures, a misalignment of only a few pixels can reduce the percentage overlap significantly. Dice coefficients measure volumetric overlaps, whereas correlation measures closeness of the numerical endpoints of organ-wise. Therefore, we would argue that these two each provide unique information about the performance of the segmentation algorithm (Dice coefficients) and its impact on the measurement endpoints (correlation).

The present study can also benefit from higher spatial resolution, which was not particularly high (5 mm across slices and 1.5–2.5 mm in-plane, within slices) in the current studies. The spatial resolutions used were chosen to facilitate repeated breathholds with two-fold accelerated parallel imaging. Consequently, deformation maps within adipose tissue depots and organs may be inaccurate due to an insufficient number of features within these regions. It is likely that registration accuracy will improve when applied to higher resolution images in which fascia, muscle bundles, and vasculature within organs are clearly visualized. We also tested the algorithm using fat fraction images instead of fat and water images separately. One disadvantage of using fat fraction images is that regions with low total signal (e.g., background, air, gas) have noisy fat fractions which confound intensity-based methods. Furthermore, regions of this type within the body are difficult to automatically identify and exclude. We also found that the use of intensity-corrected water and fat images together rather than either one in isolation, led to improved performance.

In conclusion, this study demonstrates the strong potential of automatic segmentation of 3D abdominal MRI for quantification of abdominal adipose tissue volumes and liver fat fraction. The proposed approach is potentially suitable for longitudinal studies in which a single baseline dataset can be manually analyzed in detail for each subject. We note that the evaluation in this study was based on repeated measurements, with a meal consumed between scans.

Table 4
Linear Correlation Coefficients for Adipose Tissue Volumes and Organ Fat Fractions for the REPOS and MEAL Cohorts

		SAT volume	VAT volume	Liver volume	Pancreas volume	Hepatic fat frac	Pancreas fat frac
REPOS (n=11)	Manual vs. manual	0.9994	0.9974	0.9885	0.9782	0.9996	0.9660
	Manual vs. automated	0.9493	0.9982	0.9326	0.8876	0.9972	0.8617
MEAL (n=4)	Manual vs. manual	0.9999	0.9985	0.9789	0.9765	0.99998	0.9787
	Manual vs. automated	0.9889	0.9902	0.9523	0.8760	0.9991	0.6338

Additional evaluation against manual segmentation on longitudinal data can provide more insight into the performance and suitability of the automated method for longitudinal studies. It also suggests many opportunities for future work, including improvements in intensity correction, improvements in nonrigid registration, and improvements in the automated segmentation of small organs, as well as the pursuit of registration between subjects.

REFERENCES

1. Jasik CB, Lustig RH. Adolescent obesity and puberty: the "perfect storm". Ann N Y Acad Sci 2008;1135:265–279.
2. Choudhary AK, Donnelly LF, Racadio JM, Strife JL. Diseases associated with childhood obesity. AJR Am J Roentgenol 2007; 188:1118–1130.
3. Schick F, Machann J, Brechtel K, et al. MRI of muscular fat. Magn Reson Med 2002;47:720–727.
4. Ross R, Goodpaster B, Kelley D, Boada F. Magnetic resonance imaging in human body composition research. From quantitative to qualitative tissue measurement. Ann N Y Acad Sci 2000;904: 12–17.
5. Staten MA, Totty WG, Kohrt WM. Measurement of fat distribution by magnetic resonance imaging. Invest Radiol 1989;24:345–349.
6. Fowler PA, Fuller MF, Glasbey CA, Cameron GG, Foster MA. Validation of the in vivo measurement of adipose tissue by magnetic resonance imaging of lean and obese pigs. Am J Clin Nutr 1992; 56:7–13.
7. Abate N, Garg A, Coleman R, Grundy SM, Peshock RM. Prediction of total subcutaneous abdominal, intraperitoneal, and retroperitoneal adipose tissue masses in men by a single axial magnetic resonance imaging slice. Am J Clin Nutr 1997;65:403–408.
8. Siegel MJ, Hildebolt CF, Bae KT, Hong C, White NH. Total and intraabdominal fat distribution in preadolescents and adolescents: measurement with MR imaging. Radiology 2007;242: 846–856.
9. Gronemeyer SA, Steena RG, Kauffmana WM, Reddicka WE, Glass JO. Fast adipose tissue (FAT) assessment by MRI. Magn Reson Imaging 2000;18:815–818.
10. Machann J, Thamer C, Schnoedt B, et al. Standardized assessment of whole body adipose tissue topography by MRI. J Magn Reson Imaging 2005;21:455–462.
11. Machann J, Thamer C, Stefan N, et al. Follow-up whole-body assessment of adipose tissue compartments during a lifestyle intervention in a large cohort at increased risk for type 2 diabetes. Radiology 2010;257:353–363.
12. Alabousi A, Al-Attar S, Joy TR, Hegele RA, McKenzie CA. Evaluation of adipose tissue volume quantification with IDEAL fat–water separation. J Magn Reson Imaging 2011;34:474–479.
13. Bonekamp S, Ghosh P, Crawford S, et al. Quantitative comparison and evaluation of software packages for assessment of abdominal adipose tissue distribution by magnetic resonance imaging. Int J Obes (Lond) 2008;32:100–111.
14. Tang Y, Sharma P, Nelson MD, Simerly R, Moats RA. Automatic abdominal fat assessment in obese mice using a segmental shape model. J Magn Reson Imaging 2011;34:866–873.
15. Positano V, Gastaldelli A, Sironi AM, Santarelli MF, Lombardi M, Landini L. An accurate and robust method for unsupervised assessment of abdominal fat by MRI. J Magn Reson Imaging 2004;20:684–689.
16. Peng Q, McColl RW, Ding Y, Wang J, Chia JM, Weatherall PT. Automated method for accurate abdominal fat quantification on water-saturated magnetic resonance images. J Magn Reson Imaging 2007;26:738–746.
17. Sussman DL, Yao J. Automated measurement and segmentation of abdominal adipose tissue in MRI. IEEE Int Symp Biomed Imaging 2010;936–939.
18. Zhou A, Murillo H, Peng Q. Novel segmentation method for abdominal fat quantification by MRI. J Magn Reson Imaging 2011; 34:852–860.
19. Holden M. A review of geometric transformations for nonrigid body registration. IEEE Trans Med Imaging 2008;27:111–128.
20. Johnson HJ, Christensen GE. Landmark and intensity-based, consistent thin-plate spline image registration. IEEE Trans Med Imaging 2002;21:450–461.
21. Kovacevic N, Hamarneh G, Henkelman M. Anatomically guided registration of whole body mouse MR images. Lecture notes in computer science. New York: Springer; 2003. p 870–877.
22. Pelizzari CA, Chen GT, Spelbring DR, Weichselbaum RR, Chen CT. Accurate three-dimensional registration of CT, PET, and/or MR images of the brain. J Comput Assist Tomogr 1989;13:20.
23. Park H, Bland PH, Meyer CR. Construction of an abdominal probabilistic atlas and its application in segmentation. IEEE Trans Med Imaging 2003;22:483–492.
24. Tu Z, Narr KL, Dollar P, Dinov I, Thompson PM, Toga AW. Brain anatomical structure segmentation by hybrid discriminative/generative models. IEEE Trans Med Imaging 2008;27:495–508.
25. Tu Z, Toga AW. Towards whole brain segmentation by a hybrid model. Med Image Comput Comput Assist Interv 2007;10:169–177.
26. Corso JJ, Tu Z, Yuille A, Toga A. Segmentation of sub-cortical structures by the graph-shifts algorithm. Inf Process Med Imaging 2007;20:183–197.
27. Tu Z, Zheng S, Yuille AL. Automated extraction of the cortical sulci based on a supervised learning approach. IEEE Trans Med Imaging 2007;26:541–552.
28. Zouagui T, Chereul E, Janier M, Odet C. 3D MRI heart segmentation of mouse embryos. Comput Biol Med 2010;40:64–74.
29. Ranefall P, Bidar AW, Hockings PD. Automatic segmentation of intra-abdominal and subcutaneous adipose tissue in 3D whole mouse MRI. J Magn Reson Imaging 2009;30:554–560.
30. Klein A, Ghosh SS, Avants B, et al. Evaluation of volume-based and surface-based brain image registration methods. Neuroimage 2010;51:214–220.
31. Leinhard OD, Johansson A, Rydell J, et al. Quantitative abdominal fat estimation using MRI. In: Proceedings of 19th International Conference on Pattern Recognition. 2008. p 1–4.
32. Kullberg J, Johansson L, Ahlstrom H, et al. Automated assessment of whole-body adipose tissue depots from continuously moving bed MRI: a feasibility study. J Magn Reson Imaging. 2009;30:185–193.
33. Würslin C, Machann J, Rempp H, Claussen C, Yang B, Schick F. Topography mapping of whole body adipose tissue using A fully automated and standardized procedure. J Magn Reson Imaging 2010;31:430–439.
34. Reeder SB, Pineda AR, Wen Z, et al. Iterative decomposition of water and fat with echo asymmetry and least-squares estimation (IDEAL): application with fast spin-echo imaging. Magn Reson Med 2005;54:636–644.
35. Yu H, Shimakawa A, McKenzie CA, Brodsky E, Brittain JH, Reeder SB. Multiecho water-fat separation and simultaneous R2* estimation with multifrequency fat spectrum modeling. Magn Reson Med 2008;60:1122–1134.
36. Liu CY, McKenzie CA, Yu H, Brittain JH, Reeder SB. Fat quantification with IDEAL gradient echo imaging: correction of bias from T(1) and noise. Magn Reson Med 2007;58:354–364.
37. Pruessmann KP, Weiger M, Scheidegger MB, Boesiger P. SENSE: sensitivity encoding for fast MRI. Magn Reson Med 1999;42: 952–962.
38. Jensen J, Anker C. Segmentation of abdominal adipose tissue in MRI in a clinical study of growth and diet. PhD Thesis, Technical University of Denmark, DTU Informatics; 2011.
39. Rueckert D, Sonoda LI, Hayes C, Hill DL, Leach MO, Hawkes DJ. Nonrigid registration using free-form deformations: application to breast MR images. IEEE Trans Med Imaging 1999;18: 712–721.
40. Rueckert D, Aljabar P, Heckemann RA, Hajnal JV, Hammers A. Diffeomorphic registration using B-splines. Med Image Comput Comput Assist Interv 2006;9(Pt 2):702–729.
41. Joshi AA, Shattuck DW, Thompson PM, Leahy RM. Surface constrained volumetric brain registration using harmonic mappings. IEEE Trans Med Imaging 2007;26:1657–1669.
42. Nocedal J. Updating quasi-Newton matrices with limited Storage. Math Comput 1980;35:773–782.
43. Rijsbergen CV. Information retrieval. Newton, MA: Butterworth-Heinemann; 1979.